JGR Solid Earth

RESEARCH ARTICLE
10.1029/2020JB020249

Scattering and Attenuation Characteristics at Volcanoes Inferred From Envelope Widths of Natural and Active Seismic Sources

Hiroyuki Kumagai[1], **Roberto Torres**[2], **and Yuta Maeda**[1]

[1]Graduate School of Environmental Studies, Nagoya University, Nagoya, Japan, [2]Colombian Geological Survey, Pasto, Colombia

Key Points:
- Envelope widths of natural and active seismic sources were systematically analyzed at five volcanoes
- Comparison with envelope simulations showed the existence of strong heterogeneities in a thin surface layer to 1 km depth
- Residuals between observed envelope widths and those of our estimated 1D models correlated with tomographic images

Supporting Information:
- Supporting Information S1

Correspondence to:
H. Kumagai,
kumagai@eps.nagoya-u.ac.jp

Citation:
Kumagai, H., Torres, R., & Maeda, Y. (2020). Scattering and attenuation characteristics at volcanoes inferred from envelope widths of natural and active seismic sources. *Journal of Geophysical Research: Solid Earth*, *125*, e2020JB020249. https://doi.org/10.1029/2020JB020249

Received 22 MAY 2020
Accepted 26 OCT 2020
Accepted article online 4 NOV 2020

Abstract Seismic scattering and attenuation at volcanoes, thought to be strongest on the Earth, can be used to map volcanic feeding systems. We systematically analyzed high-frequency (5–10 Hz) seismograms of volcano-tectonic earthquakes at Galeras volcano (Colombia) and active sources at Kirishima, Unzen, Bandai, and Iwate volcanoes (Japan) to investigate their scattering and attenuation characteristics. The envelope widths estimated from these seismograms were compared with those calculated by Monte Carlo envelope simulations for 1D layered models parameterized by the scattering mean free path and the quality factor of medium attenuation for *S* waves. Our results indicated a surficial, highly heterogeneous, and attenuative layer up to around 1 km thickness at all studied volcanoes. The strongest heterogeneities at volcanoes thus exist in a thin surface layer, likely comprising unconsolidated and/or highly fractured materials. Using the space-weighting function for diffusive wavefields, we mapped the residuals between observed envelope widths and those calculated with our estimated 1D models at Kirishima, Unzen, Bandai, and Iwate. These maps showed spatial distributions of the envelope-width residuals were unique to each volcano and correlated with *P* wave velocity tomographic images. Areas of positive residuals correspond to low-velocity anomalies and thus to heterogeneous, strongly scattering rocks, whereas areas of negative residuals correspond to high-velocity anomalies and thus less heterogeneous volcanic or basement rocks. Our results demonstrate that envelope widths can improve the characterization of scattering and attenuation structures beneath volcanoes.

1. Introduction

Estimation of volcano structures is fundamental to our understanding of volcanic processes related to magma ascent, gas migration, and magmatic and phreatic eruptions. Seismological studies have played an essential role in imaging volcano structures. A wide variety of *P* and *S* wave velocity (V_p and V_s, respectively) structures have been estimated at various volcanoes by tomographic methods to invert arrival times of body waves from natural and active seismic sources (e.g., Chouet & Matoza, 2013; Koulakov & Shapiro, 2015; Lees, 2007). Furthermore, temporal changes in the V_p/V_s ratios have been estimated by 4D seismic tomography (e.g., Koulakov et al., 2013; Londoño & Kumagai, 2018; Patanè et al., 2006). These studies have shown that volcanoes display seismologically detectable structural changes especially in association with magmatic intrusions.

Seismic heterogeneous characteristics beneath volcanoes are represented by the scattering mean free path (l_0) and the quality factor of medium attenuation (Q_i) for *S* waves. By fitting the seismograms excited by active sources (dynamite blasts) to those calculated with the analytical solutions of the diffusion equation or the radiative transfer theory (Paasschens, 1997) in a uniform medium or half-space, l_0 of 0.1–1 km and Q_i of 10–100 in frequency bands of 2–20 Hz have been estimated at various volcanoes (e.g., Del Pezzo et al., 2006; Friedrich & Wegler, 2005; Parsiegla & Wegler, 2008; Wegler, 2003; Wegler & Lühr, 2001; Yamamoto & Sato, 2010). These results indicate that volcanoes expose the strongest structural heterogeneities on the Earth and their seismic wavefields are dominated by multiple scattering (Sato et al., 2012). The space-weighting function (SWF) or sensitivity kernels of l_0 and Q_i for multiple scattering wavefields have been used to determine the spatial distributions of scattering and attenuation at volcanoes (e.g., Akande et al., 2019; De Siena et al., 2017; Del Pezzo et al., 2016, 2018; Gabrielli et al., 2020; Prudencio, Del Pezzo et al., 2013; Prudencio, Ibanez, et al., 2013; Prudencio et al., 2015; Prudencio, Aoki et al., 2017; Prudencio, Taira et al., 2017; Sketsiou et al., 2020).

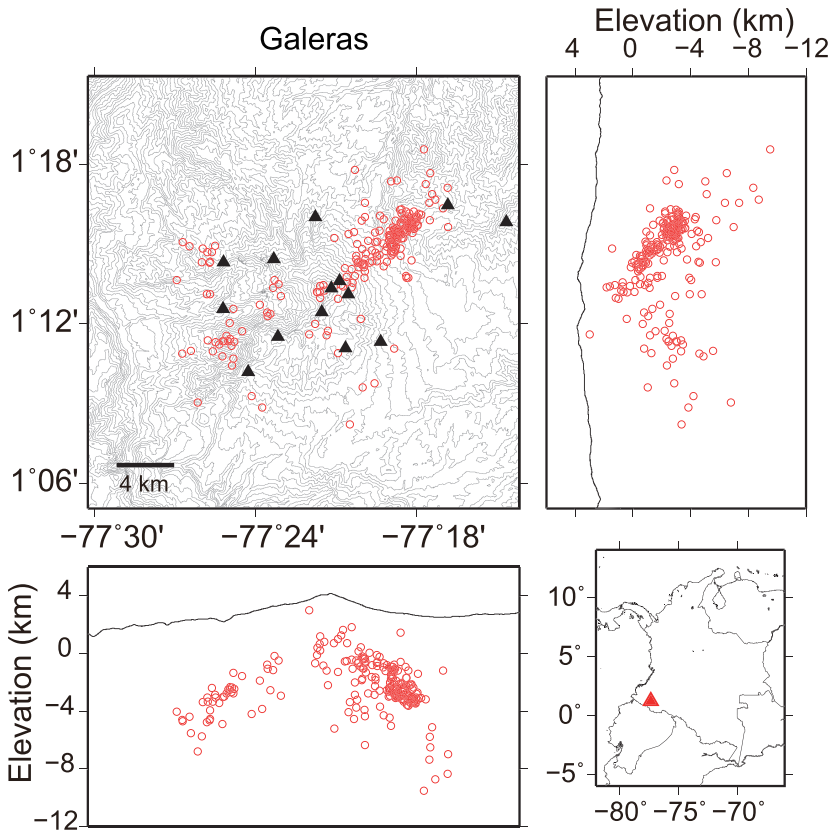

Figure 1. Topography of Galeras (200 m contour intervals), source locations of VT earthquakes (red circles), and seismic stations (black triangles). The location of Galeras is indicated by the red triangle in the regional map (bottom right).

Seismogram envelope broadening and peak delays, which have been reported for both regional tectonic earthquakes (e.g., Obara & Sato, 1995; Saito et al., 2005; Takahashi et al., 2007; Tripathi et al., 2010) and volcano-tectonic (VT) earthquakes (De Siena et al., 2016), have been explained by regional-scale heterogeneous structures. Kumagai et al. (2018) estimated envelope widths (p, the ratio of the cumulative to the peak amplitude for S waves in high-frequency [5–10 Hz] seismograms) of VT earthquakes at Nevado del Ruiz (Colombia) and Taal (Philippines) and compared them to those calculated by Monte Carlo envelope simulations following the method of Yoshimoto (2000) for layered l_0 and Q_i models. They showed that a highly heterogeneous and attenuative layer at these volcanoes exists only to 1 km depth, below which l_0 and Q_i are similar to those in the normal crust. Such a strongly heterogenous surface layer was also reported by Wegler (2004) at Vesuvius volcano (Italy) based on comparison of seismograms produced by active sources with the analytical solution of the diffusion equation in a surface layer over a uniform half-space. These studies suggest that l_0 and Q_i structures are strongly depth dependent at volcanoes, far from the uniform l_0 and Q_i distributions assumed in most previous studies using the analytical solutions. Therefore, further studies are required to estimate 1D l_0 and Q_i structures at other volcanoes and to develop a method for investigating their 3D distributions, which will improve our understanding of magmatic and hydrothermal systems.

Table 1
One-Dimensional P Wave Velocity Structure Used in Our Hypocenter Determinations at Galeras

Depth (km)	*P* wave velocity (m/s)
−5.5	3,500
−2.2	3,700
−0.2	4,000
3.8	6,000
21.8	6,800

Recently, the amplitude source location (ASL) method (Battaglia & Aki, 2003; Kumagai et al., 2010; Yamasato, 1997) and the seismic amplitude ratio method (Taisne et al., 2011) have been widely used to determine the source locations of long period (LP) and very long period (VLP) events and tremor with emergent onsets (e.g., Caudron et al., 2018; Ichihara & Matsumoto, 2017; Ichimura et al., 2018; Kumagai et al., 2013; Kurokawa et al., 2016; Maeda et al., 2019; Mori & Kumagai, 2019; Ogiso & Yomogida, 2015;

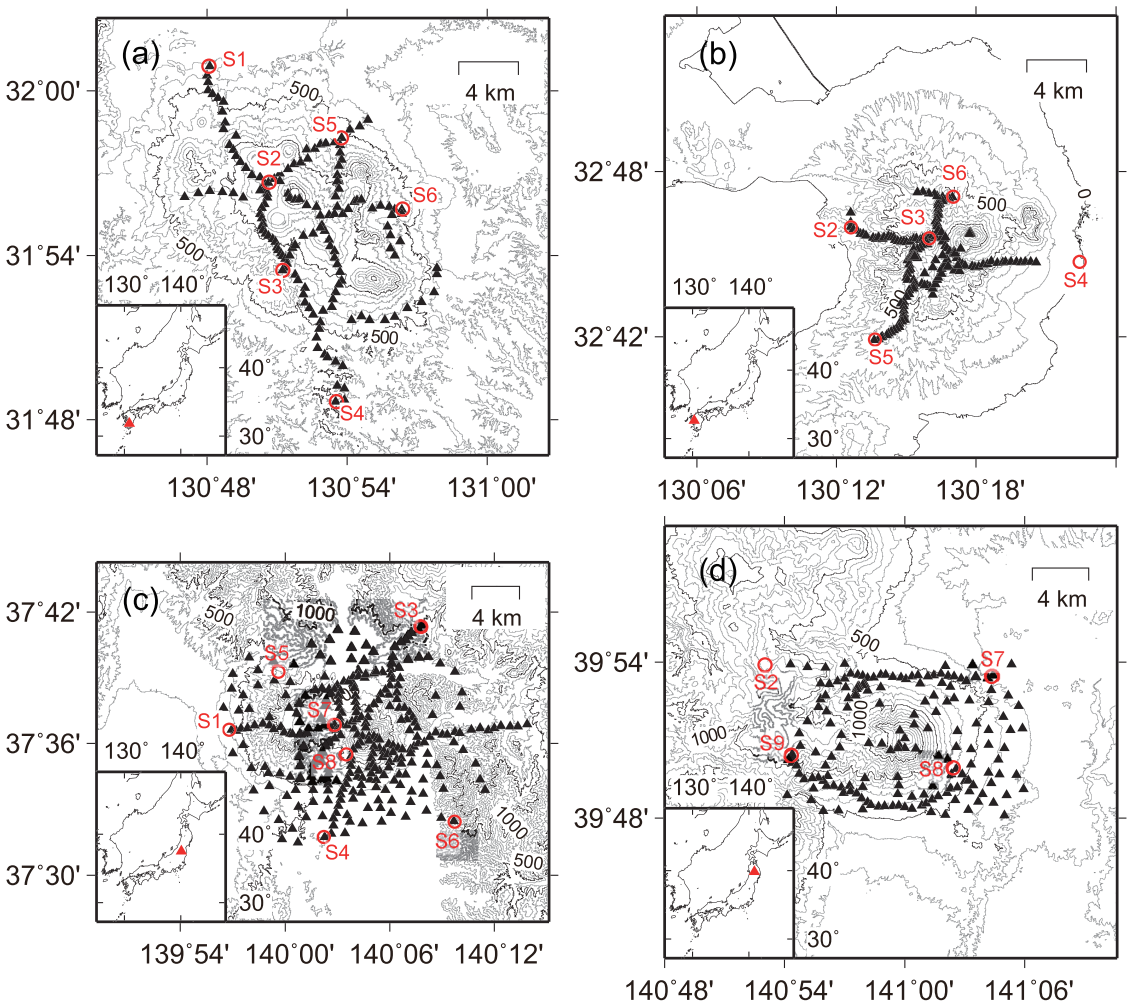

Figure 2. Topography (100 m contour intervals) and temporary seismic stations (black triangles) at (a) Kirishima, (b) Unzen, (c) Bandai, and (d) Iwate. Red circles indicate the epicenters of active sources produced by dynamite blasts, and the red labels (S1, S2, etc.) indicate the shot number. The locations of Kirishima, Unzen, Bandai, and Iwate are shown by red triangles in the inset regional maps.

Pérez-Guillén et al., 2019; Tan et al., 2019; Walter et al., 2017). As the assumption of isotropic radiation of *S* waves used in these methods holds for strong structural heterogeneities at volcanoes (Morioka et al., 2017), accommodating depth-dependent scattering and attenuation structures contributes to improving the accuracy of ASL estimates and hence seismic monitoring of active volcanism (Kumagai et al., 2019).

In this paper, we applied the method of Kumagai et al. (2018) based on envelope widths to VT earthquakes at Galeras volcano (Colombia) and active sources at Kirishima, Unzen, Bandai, and Iwate volcanoes (Japan) to estimate their 1D l_0 and Q_i structures. Our results confirm that a highly heterogenous and attenuative surface layer commonly exists to a depth of around 1 km beneath these volcanoes. We used the 2D SWF of Del Pezzo et al. (2016) to map the distributions of the residuals between observed envelope widths and those calculated with 1D models (Δp) at Kirishima, Unzen, Bandai, and Iwate and found that the Δp distributions correlate with tomographic images. We discuss the similarity and diversity in our estimated 1D structures and Δp distributions and their relations to volcanic structures.

2. Data and Methods

2.1. VT Earthquakes at Galeras

Galeras in Colombia (Figure 1) is an active andesitic volcano producing repetitive dome-forming and Vulcanian eruptions (e.g., Bain et al., 2019; Calvache & Williams, 1997) accompanied by VT earthquakes,

Table 2
Parameter Values Used in Our Monte Carlo Simulations

Parameter	Value
r_0	0.1, 0.5, 1.0,..., 13.5, 14.0 km
Δr	50 m
Δz	100 m
Δt	0.02 s
f	7.5 Hz

LP events, and tremor (e.g., Gil Cruz & Chouet, 1997; Stix et al., 1997; Torres et al., 1996). For our analysis, we used VT earthquakes observed by broadband and short-period seismometers at Galeras between April 2015 and February 2019 (Figure 1). No eruptions occurred during this period, but a swarm of VT earthquakes occurred during May–July 2018. Following Kumagai et al. (2018), we determined hypocenters and origin times by the method of Benz et al. (1996) based on the finite-difference method of Podvin and Lecomte (1991) to calculate traveltimes of first-arrival waves. Table 1 lists the velocity model in our hypocenter determinations.

2.2. Active Sources at Kirishima, Unzen, Bandai, and Iwate

Kirishima (Kyushu, southwestern Japan) is a volcanic complex, where sub-Plinian eruptions occurred at Shimoe-dake during 26–27 January 2011 (Ichihara, 2016; Kozono et al., 2014; Nakada et al., 2013; Shimbori et al., 2013). Unzen (Kyushu) produced dome-forming eruptions accompanied by deadly pyroclastic flows at Fugen-dake in June 1991 (Nakada et al., 1999; Sato et al., 1992; Yamasato et al., 1993). Bandai is a stratovolcano in northeastern Japan, at which a phreatic eruption triggered a large sector collapse in 1888 (Nakamura, 1978; Sekiya & Kikuchi, 1889). Iwate (northeastern Japan) became active in 1998 with VT earthquakes, LP and VLP events, tremor, and crustal deformation (Miura et al., 2000; Nishimura et al., 2000; Tanaka, Hamaguchi, Yamawaki et al., 2002), although no eruptions followed.

For our analyses at these volcanoes, we used active sources produced by dynamite blasts at Kirishima in 1994 (Kagiyama et al., 1995; Matsushima et al., 1995; Tomatsu et al., 1997, 2001; Tsutsui et al., 1996), Unzen in 1995 (Matsushima et al., 1997; Nishi, 2002), Bandai in 1997 (Yamawaki et al., 2004), and Iwate in 2000 (Tanaka, Hamaguchi, Yamawaki et al., 2002; Tanaka, Hamaguchi, Nishimura, et al., 2002) (Figure 2). These seismic explorations were conducted by the Japanese national project to better understand volcano structures (Kagiyama et al., 1995). More than 100 short-period seismometers with local data loggers were temporarily deployed to observe earthquakes excited by chemical explosions at each volcano (Figure 2), and their detailed V_p structures were estimated (Nishi, 2002; Tanaka, Hamaguchi, Nishimura, et al., 2002; Tomatsu et al., 1997, 2001; Tsutsui et al., 1996; Yamawaki et al., 2004). In our analyses of the envelope widths of active sources at these volcanoes, we excluded some explosions located far from the volcanic centers, and some stations very close to sea level because they may not provide accurate structural information.

2.3. Envelope Widths

We used the method of Kumagai et al. (2018) to estimate envelope widths of VT earthquakes at Galeras and active sources at Kirishima, Unzen, Bandai, and Iwate. We measured *P* wave arrival times of VT earthquakes at Galeras and used those reported by Kagiyama et al. (1995) at Kirshima, Matsushima et al. (1995) at Unzen, Yamawaki et al. (2004) at Bandai, and Tanaka et al. (2002) at Iwate. We obtained envelope waveforms from vertical band-passed (5–10 Hz) seismograms. We measured the peak amplitude (A) in the envelope waveform after the *S* wave arrival time. Noise portions before the *P* wave arrival time in the time-integrated envelope waveform were used to estimate the linear trend. We estimated the offset of the integrated waveform from the trend line at the end of coda wave arrivals (I_e) and that at the *S* wave arrival time (I_p) to obtain the cumulative amplitude $I = I_e - I_p$ (see Kumagai et al., 2018, for more details). The envelope width was estimated as $p = I/A$.

Table 3
One-Dimensional S Wave Velocity Structure Used in Our Monte Carlo Simulations

Depth (km)	*S* wave velocity (m/s)
0.0	1,750
1.0	2,250
4.0	3,000
15.0	3,500

2.4. Monte Carlo Envelope Simulations

We simulated envelope waveforms in depth-dependent l_0 and Q_i structures using the method of Yoshimoto (2000). Following Kumagai et al. (2018), we assumed scalar *S* waves, a linear increase of V_s with depth, and constant l_0 and Q_i values in each layer. Each particle isotropically radiated from a source moves over distance $V_s\Delta t$ without scattering for a time step Δt, and its energy attenuates by $\exp(-2\pi f\Delta t/Q_i)$, where f is frequency. The particle changes the propagation direction with the probability given by $V_s\Delta t/l_0$. We used 3D domains with horizontal dimensions of 32 × 32 km and vertical dimensions of 15 km for Galeras and 5 km for

Table 4
Values of Scattering Mean Free Path (l_0), the Quality Factor of Medium Attenuation for S Waves (Q_i), and Layer Depths Used for Trial Models in Our Monte Carlo Simulations for Galeras

Layer number	Layer boundary depth (km)	l_0 (km)	Q_i
1	1.0	0.5, 1, 10	50, 100, 200
2	5.0	1, 10, 100, 1,000	100, 200, 300
3	15.0	10, 100, 1,000	100, 200, 300

the other volcanoes, in which absorbing boundary conditions were used except for a free flat surface. We assumed three- and two-layered structures at Galeras and the other volcanoes, respectively. Assuming radial symmetry, we set receivers at equal distances from the epicenter, and we accumulated energy particles that reached the receiver volume defined by $r_0 \pm \Delta r$ and Δz in the radial and vertical directions, respectively, where r_0 is the radius from the epicenter. We used source depths of 1.5, 4.5, and 7.5 km for Galeras and 50 m for the other volcanoes. In our Monte Carlo simulations, we used the parameter values listed in Table 2, various l_0 and Q_i values and layer boundary depths (see section 2.5), and linearly interpolated V_s structures using the V_s values listed in Table 3. The Monte Carlo method of Yoshimoto (2000) does not include surface waves. The dominance of *S* waves in seismograms in a high-frequency band of 5–10 Hz has been indicated by the finite-difference full-waveform simulation study of Morioka et al. (2017) as well as ASL studies assuming isotropic radiation of *S* waves (e.g., Battaglia & Aki, 2003; Kumagai et al., 2010, 2019; Ogiso & Yomogida, 2015). Therefore, our use of the Monte Carlo simulations without including surface waves is justified.

2.5. Model Estimates

We exactly followed the grid-search approach of Kumagai et al. (2018) to obtain the best fitting layered model at Galeras. Observed envelope widths were divided into source depth ranges of 0–3, 3–6, and 6–9 km denoted as $n = 1, 2$, and 3, respectively. The simulated envelope widths estimated from envelope simulations at source depths of 1.5, 4.5, and 7.5 km were fit to the observed envelope widths in the respective depth ranges using the polynomial function:

$$p_n^k(r) = \sum_{j=1}^{m} {}_k a_n^j r^j, \tag{1}$$

where r is source-station distance, p_n^k represent the simulated envelope widths, ${}_k a_n^j$ are coefficients for the polynomial function of the nth depth range in the kth model, and m is the polynomial order. We used the following normalized residuals:

$$R_n^k = \frac{\sum_{l=1}^{N} \left\{ p_n^o(r_l) - p_n^k(r_l) \right\}^2}{\sum_{l=1}^{N} \left\{ p_n^o(r_l) \right\}^2}, \tag{2}$$

where r_l is the source-station distance of the lth data points, p_n^o is the observed envelope widths in the nth depth range, and N is the number of data points. We evaluated the total normalized residual as R^k

Table 5
Values of Scattering Mean Free Path (l_0), the Quality Factor of Medium Attenuation for S Waves (Q_i), and Layer Boundary Depths Used for Trial Models in Our Monte Carlo Simulations for Kirishima, Unzen, Bandai, and Iwate

Layer number	Layer boundary depth (km)	l_0 (km)	Q_i
1	0.5, 0.75, 1.0, 1.25	0.25, 0.5, 1, 10	10, 25, 50, 100, 200
2	5.0	1, 10, 100, 1,000, 5,000	25, 50, 100, 200

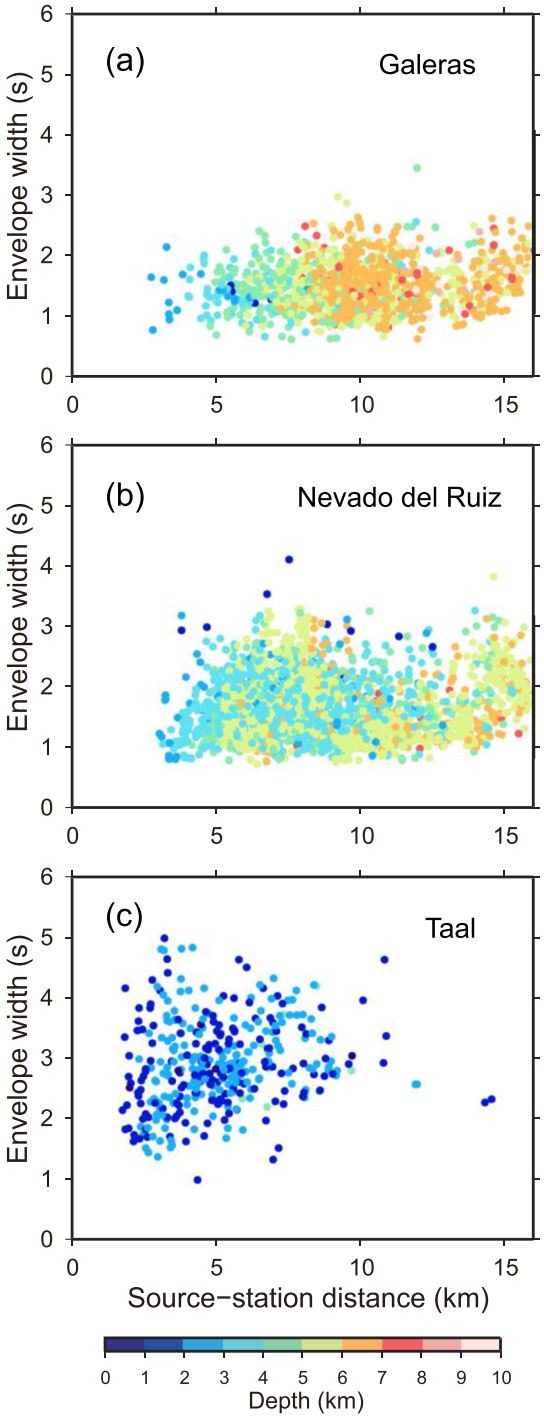

Figure 3. Envelope widths of VT earthquakes plotted against source-station distances at (a) Galeras, (b) Nevado del Ruiz, and (c) Taal (data at Nevado del Ruiz and Taal are from Kumagai et al., 2018). Source depths, measured from 3.4 and 4.4 km above sea level at Galeras and Nevado del Ruzi, respectively, and sea level at Taal, are shown by the color scale.

$= \left(R_1^k + R_2^k + R_3^k\right)/3$. Three layers with boundaries at depths of 1, 5, and 15 km with l_0 and Q_i values increasing in deeper layers were assumed (Table 4). We adopted combinations of l_0 and Q_i values in the three layers that provided $R^k < 0.5$. Using these combinations, we adjusted the boundary depth between the first and second layers to either 0.5 or 2 km and that between the second and third layers to either 4 or 6 km. We estimated the averaged l_0 and Q_i model as

$$\bar{l}_0 = \frac{\sum_{k=1}^{M} w_k l_0^k}{\sum_{k=1}^{M} w_k}, \quad \overline{Q}_i = \frac{\sum_{k=1}^{M} w_k Q_i^k}{\sum_{k=1}^{M} w_k}. \tag{3}$$

Here l_0^k and Q_i^k are l_0 and Q_i in each layer for the kth model, $w_k = e^{-R^k}$, and M is the number of models. The layer boundary depths were estimated as the weighted averages of the adjusted depths.

At Kirishima, Unzen, Bandi, and Iwate, we followed the same procedure but used only one depth range (0–3 km) for the observed envelope widths and two layers (trial l_0 and Q_i values and boundary depths are listed in Table 5) and a source depth of 50 m in the Monte Carlo simulations. We conducted a grid search for the trial models to evaluate $R^k = R_1^k$ at each volcano. We estimated the averaged models by using Equation 3 with the layer boundary depths taken as the weighted averages of those determined for the individual volcanoes.

3. Results

3.1. Observed Envelope Widths

Observed envelope widths at Galeras were smaller than those estimated at Nevado del Ruiz and Taal (Figure 3). Although the envelope widths at Galeras did not obviously increase up to r of around 5 km as observed at Nevado del Ruiz and Taal, nearly constant values were observed at larger distances at all three volcanoes. As shown by Kumagai et al. (2018), the envelope width increases monotonically with increasing r when uniform distributions of l_0 and Q_i are assumed. Therefore, a depth-dependent structure is required to explain the observed envelope widths at Galeras.

Observed envelope widths at Kirishima, Unzen, Bandai, and Iwate (Figure 4) generally increased up to r of around 5 km, and then they were nearly constant or slightly increased. Data scatter along the trends was largest at Iwate and least at Bandai.

We note that envelope widths depend on the source-station distance as well as the source depth as indicated by Kumagai et al. (2018). The observed envelope widths at Kirishima, Unzen, Bandai, and Iwate were relatively larger than those at Galeras at the same source-station distance (Figures 3a and 4). The sources of VT earthquakes that we used at Galeras (Figure 1) were deeper than the active sources at Kirishima, Unzen, Bandai, and Iwate (Figure 2). These shallow active sources were strongly affected by shallow heterogenous layers, which resulted in larger envelope widths.

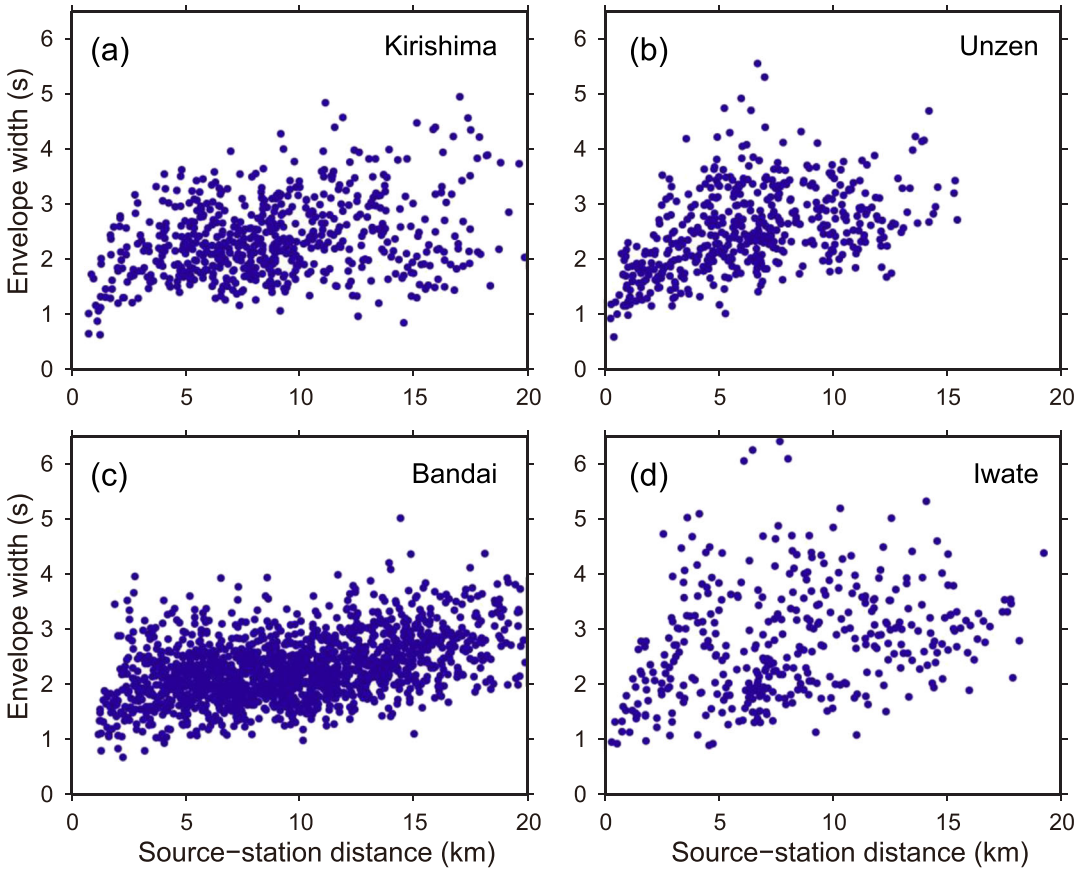

Figure 4. Envelope widths of active sources plotted against source-station distance at (a) Kirishima, (b) Unzen, (c) Bandai, and (d) Iwate.

3.2. One-Dimensional Models

Our results of the grid search using polynomial order $m = 3$ at Galeras are shown in Figure S1 in the supporting information. This polynomial order was used at Taal and Nevado del Ruiz (Kumagai et al., 2018) and provided the minimum R^k values compared with those of other orders at Galeras. Using the envelope widths of models with residuals within 1.1 times the minimum R^k values (green lines in Figure 5), we obtained the averaged l_0 and Q_i models shown in Figure 6 and listed in Table 6. Our estimated structures at Galeras indicated that the first layer was 0.5 km thick with $l_0 = 710$ m and $Q_i = 120$, whereas l_0 was larger than 10^2 km and Q_i was around 100–200 in the second and third layers.

Our results of the grid search with $m = 5$ at Kirishima, Unzen, Bandai, and Iwate are shown in Figures S2–S5 and Table S1. We used $m = 5$ because the residuals were minimized at this order or did not change greatly when higher orders were used (Figure S6). Using the envelope widths of models with residuals within 1.1 times the minimum R^k values (green lines in Figure 7), we obtained the averaged models shown in Figure 8 and listed in Table 6. Our estimated models at these volcanoes were very similar: The first layers were 600–900 m thick with $l_0 = 250$ m and Q_i around 25, and the second layers had l_0 around 10^3 km and Q_i around 50–70. We note that $l_0 = 250$ m was the minimum value explored in our trial models because of the long computational times required in the Monte Carlo simulations of such strongly scattering media. It is therefore possible that l_0 in the first layer could be smaller than our estimates, although our estimations reasonably fit the observed trends at these volcanoes (Figure 7).

3.3. Mapping of Envelope Width Residuals

The 2D SWF (Del Pezzo et al., 2016), derived from energy distributions in diffusive wavefields, is given as

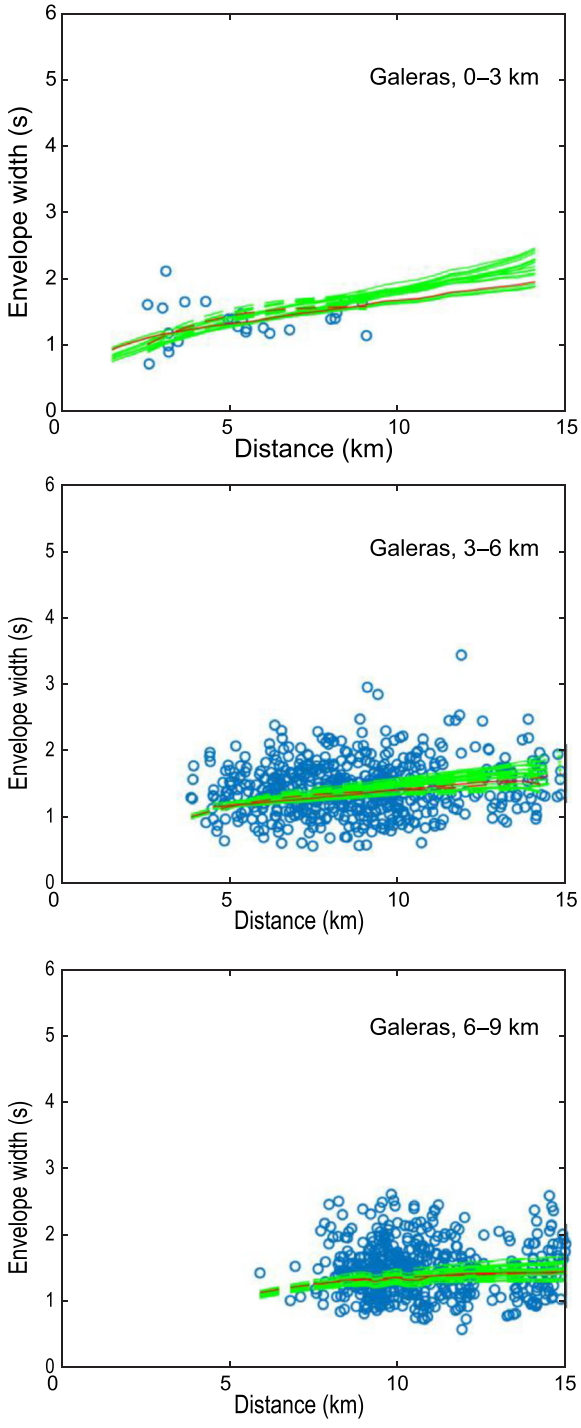

Figure 5. Observed and simulated envelope widths at Galeras. Blue circles indicate observed envelope widths for VT earthquakes in three source-depth ranges. Red solid and dashed lines are the envelope widths simulated by the model with the minimum residual and their fits by Equation 1, respectively. Green solid and dashed lines are the envelope widths of models with residuals within 1.1 times the minimum residual and their fits by Equation 1, respectively.

$$\kappa_l^k(x,y) = \frac{1}{2\pi\sigma_x\sigma_y}\exp\left[-\left\{\frac{(x-x_l)^2}{2\sigma_x^2}+\frac{(y-y_l)^2}{2\sigma_y^2}\right\}\right] + \frac{1}{2\pi\sigma_x\sigma_y}\exp\left[-\left\{\frac{(x-x_k)^2}{2\sigma_x^2}+\frac{(y-y_k)^2}{2\sigma_y^2}\right\}\right] + \frac{1}{4\pi\sigma_x\sigma_y}\exp\left[-\left\{a(x-x_0)^2+2b(x-x_0)(y-y_0)+c(y-y_0)^2\right\}\right] \quad (4)$$

Here

$$a = \frac{\cos^2\theta}{12\sigma_x^2}+\frac{\sin^2\theta}{2\sigma_y^2},\quad b = -\frac{\sin 2\theta}{24\sigma_x^2}+\frac{\sin 2\theta}{4\sigma_y^2},\quad c = \frac{\sin^2\theta}{24\sigma_x^2}+\frac{\cos^2\theta}{2\sigma_y^2}, \quad (5)$$

$$\sigma_x = \delta_x d,\ \sigma_y = \delta_y d,\ x_0 = \frac{x_k+x_l}{2},\ y_0 = \frac{y_k+y_l}{2}, \quad (6)$$

where x and y are the Cartesian coordinates; (x_k, y_k) and (x_l, y_l) are source and receiver locations, respectively; d is the source-station distance; $\delta_x = \delta_y = 0.2$; and $\theta = \tan^{-1}\{(y_k - y_l)/(x_l - x_k)\}$. Although the SWF was only given by Del Pezzo et al. (2016) for sources and stations positioned on the x-axis, they actually used the general form for the arbitrary source and station positions given in Equation 4. Because the sources and stations were located in the first heterogenous layer at Kirishima, Unzen, Bandai, and Iwate, and because the scatter in observed envelope widths is sensitive to the first layer (Kumagai et al., 2018), the SWF can be used to map the individual residual values between the observed envelope widths and those calculated with the best fit layered model (Table S1) at each volcano. However, the SWF may not be used for the envelope-width residuals at Galeras, Taal, or Nevado del Ruiz, because the sources are located in the second and third less heterogeneous layers and the diffusive wavefields between the sources and stations are not entirely established.

Following Sketsiou et al. (2020), we used both a regionalization approach and a tomography approach to map the envelope-width residuals using the SWF. In the regionalization approach, we estimated the distributions of spatially weighted envelope-width residuals defined as

$$W(n_x,n_y) = \sum_{l=1}^{N_l}\sum_{k=1}^{N_k} P_l^k(n_x,n_y)/(\Delta x\Delta y), \quad (7)$$

where

$$P_l^k(n_x,n_y) = K_l^k(n_x,n_y)\Delta p_l^k \quad (8)$$

$$K_l^k(n_x,n_y) = \frac{\kappa_l^k(n_x,n_y)}{\sum_{i=1}^{N_x}\sum_{j=1}^{N_y}\kappa_l^k(i,j)}. \quad (9)$$

Here Δp_l^k is the envelope-width residual for the lth event at the kth station; N_k and N_l are the numbers of stations and events, respectively; n_x and n_y represent the grid points; N_x and N_y are the numbers of grid points in the x and y directions, respectively; and Δx and Δy are the grid intervals in the x and y directions, respectively. In the tomography

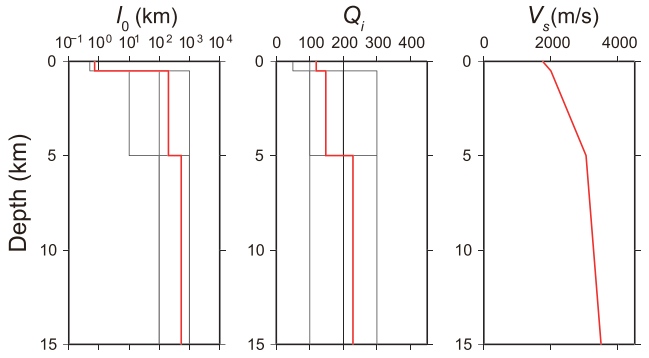

Figure 6. Estimated models with residuals within 1.1 times the minimum residual (black lines) and the averaged model (red line), respectively, at Galeras.

approach, we solved the following observation equation to estimate $P_l^k(n_x, n_y)$ by the damped least squares method (e.g., Menke, 1989):

$$\mathbf{d} = \mathbf{Am} \tag{10}$$

where

$$\mathbf{d} = \left[\Delta p_1^1 \cdots \Delta p_{N_l}^{N_k} 0 \cdots 0\right]^T, \tag{11}$$

$$\mathbf{A} = \begin{bmatrix} K_1^1(1,1) & \cdots & \cdots & K_1^1(N_x,N_y) \\ \vdots & \ddots & & \vdots \\ \vdots & & \ddots & \vdots \\ K_{N_l}^{N_k}(1,1) & \cdots & \cdots & K_{N_l}^{N_k}(N_x,N_y) \\ \lambda & 0 & \cdots & 0 \\ \vdots & \ddots & & \vdots \\ \vdots & & \ddots & 0 \\ 0 & \cdots & 0 & \lambda \end{bmatrix}, \tag{12}$$

$$\mathbf{m} = \left[P_1^1(1,1) \cdots P_{N_l}^{N_k}(N_x,N_y)\right]^T. \tag{13}$$

Here T denotes transpose and λ is the damping factor.

At each volcano, we plotted Δp_l^k along each ray path (Figure 9) and the number of rays in each grid with $\Delta x = \Delta y = 500$ m (Figure S7). We also constructed envelope-width residual maps by the regionalization and tomography approaches (Figures 10 and 11, respectively). In the tomography approach, we used $\lambda = 0.2$ at all four volcanoes (Figure S8). The maps obtained by the two approaches at the individual volcanoes display similar positive and negative locations, but the short-wavelength patterns are enhanced in the maps obtained by the tomography approach. As discussed by Sketsiou et al. (2020), the regionalization approach tends to be affected by greatly deviated data or outliers. The differences in our maps obtained by the two approaches may be caused by such effects. In the following discussion, we use the maps obtained by the tomography approach (Figure 11).

At Kirishima, areas of positive residuals were located near the two shot positions (S1 and S5), whereas areas of negative residuals were located near the other shot positions (S2, S3, and S6) (see shot positions in Figure 2). Areas of positive residuals also existed near the summits of Shimoe-dake and Ohachi. At Unzen, an area of strong negative residuals existed beneath the western flank. At Bandai, areas of negative residuals were near some shot positions (S3, S4, and S5) and beneath the volcanic center and an area of positive residuals existed beneath the southeastern flank. At Iwate, broad areas of positive and negative residuals existed along the eastern and western flanks, respectively.

Table 6
Averaged Models of the Scattering Mean Free Path (l_0) and the Quality Factor of Medium Attenuation for S Waves (Q_i) at Galeras, Kirishima, Unzen, Bandai, and Iwate Volcanoes

Volcano	Layer boundary depth (km)	l_0 (km)	Q_i
Galeras	0.5	0.71	120
	5.0	200	150
	15.0	530	230
Kirishima	0.69	0.25	25
	5.0	2,000	50
Unzen	0.83	0.25	25
	5.0	2,000	72
Bandai	0.58	0.25	25
	5.0	2,000	50
Iwate	0.91	0.25	27
	5.0	1,900	66

4. Discussion

Our grid search results of the observed envelope widths indicated that a highly heterogeneous and attenuative surface layer exists to around 1 km depth at all studied volcanoes (Figures 6 and 8). Although the envelope-width residuals mapped using the 2D SWF display various spatial distributions at Kirishima, Unzen, Bandai, and Iwate (Figure 11), our estimated 1D models are similar to those at Vesuvius (Wegler, 2004), Nevado del Ruiz, and Taal (Kumagai et al., 2018). These results clearly indicate that strong heterogeneities at volcanoes are surface characteristics.

The values of l_0 and Q_i estimated in the first layer for the VT earthquakes and active sources were systematically different: l_0 = 700–1,000 m and Q_i = 100–200 at Galeras, Nevado del Ruiz, and Taal (VT earthquakes)

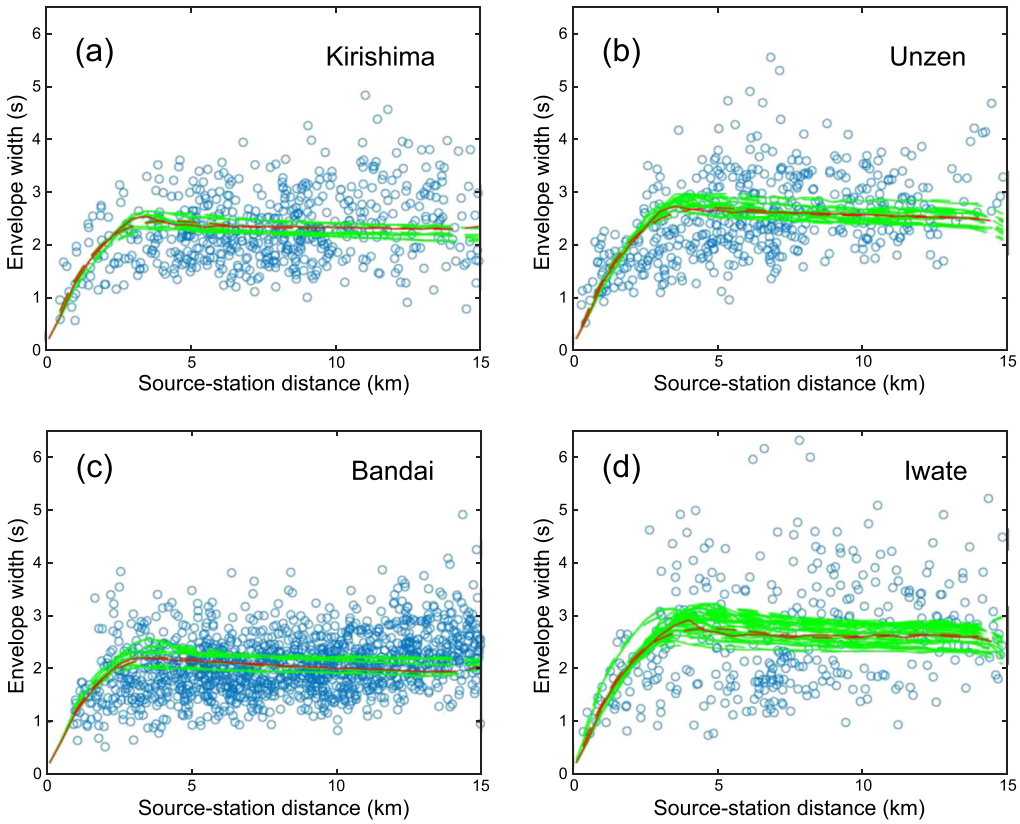

Figure 7. Observed and simulated envelope widths at (a) Kirishima, (b) Unzen, (c) Bandai, and (d) Iwate. Symbols as in Figure 5.

and $l_0 = 250$ m and Q_i of around 25 at Kirishima, Unzen, Bandai, and Iwate (active sources); the estimated l_0 and Q_i values in the second layer were also systematically different (Figure 12). These systematic differences may result from the different resolutions attained for VT earthquakes and active sources. For natural earthquakes, the observed envelope widths were divided into source-depth ranges of 0–3, 3–6, and 6–9 km for comparison with those calculated for various structures at depths of 1.5, 4.5, and 7.5 km. We used this approach because all possible combinations of source-station pairs were not practical to compute in our grid search by the Monte Carlo method, because it would require extensive computational time. Therefore, the 1D models estimated from natural earthquakes may be poorly resolved, especially at shallow depths, where fewer earthquakes occurred. On the other hand, the active sources were located at shallow depths of around 50 m. There may be depth-dependent structures within the first layer; particularly, the upper most part may be highly heterogeneous and attenuative. Therefore, the results from active sources may be strongly affected by this uppermost part of the first layer, which also affected estimates in the second layer. Despite such systematic differences, our results clearly show that a thin, surficial, heterogeneous layer underlain by less heterogenous layers is a common feature. As discussed by Kumagai et al. (2018), this surface layer may correspond to low-velocity surface layers commonly observed in tomographic images (e.g., Aoki et al., 2009; Molina et al., 2005; Nishi, 2002; Tanaka, Hamaguchi, Nishimura, et al., 2002; Tomatsu et al., 2001; Yamawaki et al., 2004; Zollo et al., 2003) and low-resistivity surface layers inferred from electromagnetic surveys at various volcanoes (e.g., Aizawa et al., 2008; Alanis et al., 2013; Kanda et al., 2008; Nurhasan et al., 2006; Yamaya et al., 2013). This layer may consist of unconsolidated and/or highly fractured materials, hydrothermal fluids, and altered clay minerals, all of which are common to volcanic edifices and produce strongly scattering wavefields.

At Galeras, 3D distributions of scatterers estimated by Carcolé et al. (2006) using the method of Nishigami (1991) and assuming single scattering indicate that strong scattering regions are broadly

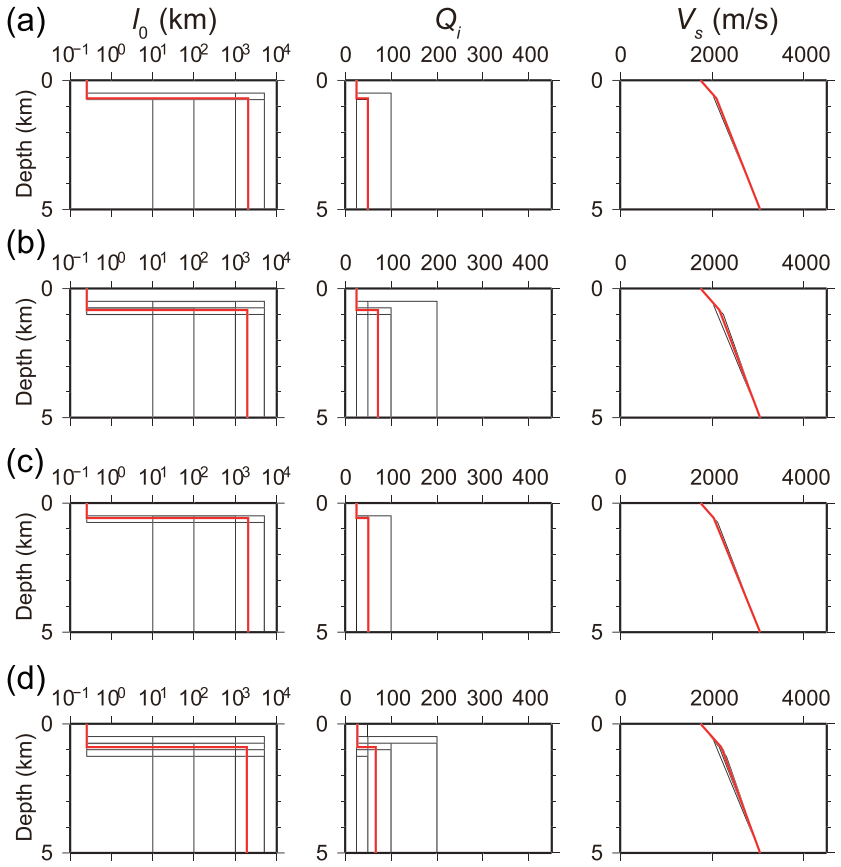

Figure 8. Estimated models at (a) Kirishima, (b) Unzen, (c) Bandai, and (d) Iwate. Symbols as in Figure 6.

distributed beneath the summit at depths between 4 and 8 km. However, we do not observe this feature in our estimated 1D model at Galeras. This difference is likely due to their assumption of single scattering, which is inappropriate at Galeras because of the dominance of multiple scattering, especially at shallow depths in volcanic edifices.

Although the 1D models estimated at Kirishima, Unzen, Bandai, and Iwate were quite similar, the scatter in the observed envelope widths showed different features among these volcanoes (Figures 4 and 7). The observed envelope widths at Bandai were less scattered than those at the other volcanoes, of which Iwate showed the broadest scatter. Their envelope-width residual maps clearly show different spatial distributions (Figure 11). Despite the less scattered envelope widths at Bandai, distinct areas of negative and positive residuals were observed there (Figure 11c). At Iwate, the scattered envelope-width residuals appeared as broad areas of positive and negative residuals in the edifice (Figure 11d). Negative and positive residuals were distributed in the volcano flanks at Kirishima (Figure 11a), and an area of strong negative residuals existed at Unzen (Figure 11b).

Positive (negative) envelope-width residuals represent smaller l_0 (larger) and/or larger (smaller) Q_i values from the 1D model (Kumagai et al., 2018). In other words, positive residuals indicate more heterogeneous and/or less attenuative bodies and negative residuals less heterogeneous and/or more attenuative bodies. Indeed, we noted correlations between our residual maps and 3D V_p tomographic images from previous studies at these volcanoes (Nishi, 2002; Tanaka, Hamaguchi, Nishimura, et al., 2002; Tomatsu et al., 2001; Yamawaki et al., 2004). Comparison of our map at Kirishima (Figure 11a) and the P wave velocity image of Tomatsu et al. (2001) at depths between −1.5 and −0.5 km below sea level (Figures 10a and 10b of Tomatsu et al., 2001) indicates that the areas of positive residuals observed near shot locations S1 and S5 (Figure 2a) and the summit of Shimoe-dake correspond to low velocities of around $V_p = 2$ km/s. We also found at Kirishima that the areas of negative residuals near shot locations S2 and S6 correspond to high

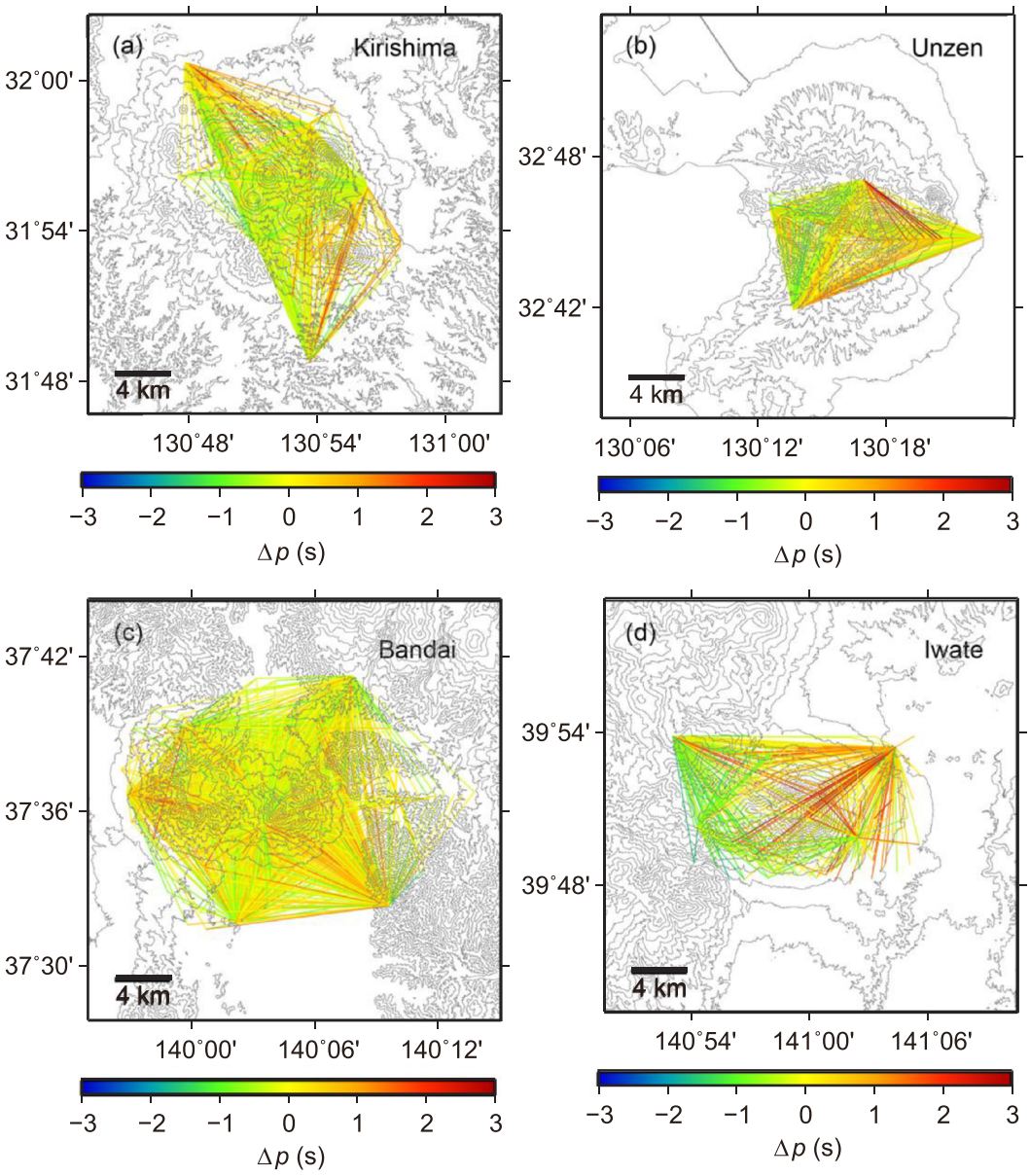

Figure 9. Envelope-width residuals (Δ*p*, the residuals between the observed envelope widths and those calculated with the best-fit layered model) plotted along ray paths using the color scale shown at the bottom of each map: (a) Kirishima, (b) Unzen, (c) Bandai, and (d) Iwate.

velocities and that near S3 corresponds to low velocities. At Unzen, the clear area of negative residuals in the western flank (Figure 11b) corresponds to high velocities around $V_p = 5$ km/s at depths between 0 and 1 km below sea level (Figures of 7a and 7b of Nishi, 2002), which were interpreted as pre-Unzen volcanic rock based on the geological map of Hoshizumi et al. (1999). We also note an area of positive residuals around Fugen-dake (Figure 11b), where the 1991 Unzen eruptions occurred. At Bandai, areas of negative residuals at shot locations S3, S4, and S5 and in the volcanic center and the area of positive residuals in the southeastern flank (Figures 2c and 11c) correspond to high- and low-velocity anomalies, respectively, at depths between −1 and 1 km below sea level in tomographic images (see Figures 9a–9c of Yamawaki et al., 2004). Although the tomographic images at Iwate of Tanaka, Hamaguchi, Nishimura, et al. (2002) were shown only in limited plan view and cross section, they indicate low- and high-velocity anomalies at

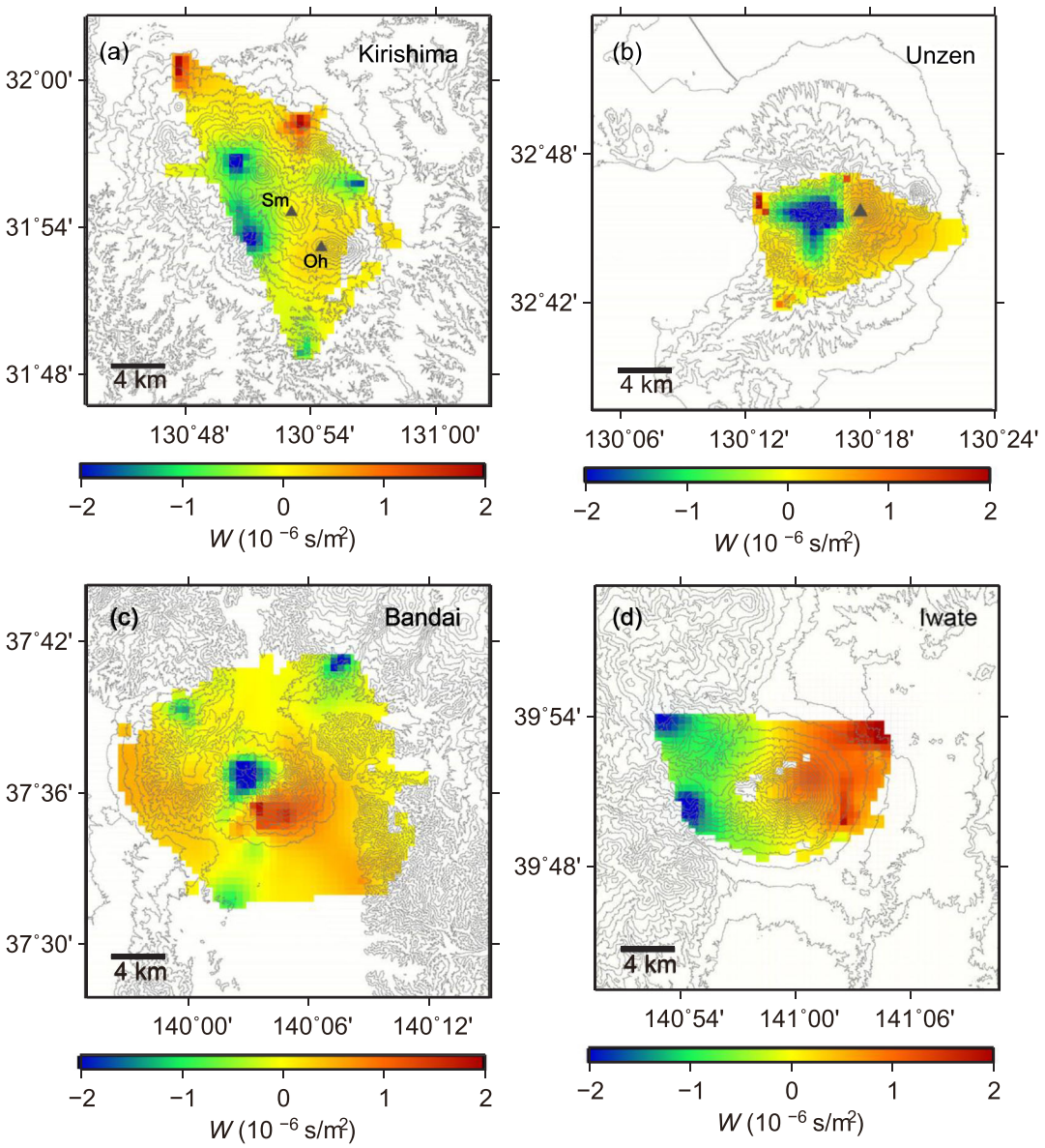

Figure 10. Envelope-width residual maps based on the regionalization approach using Equations 7 and 8 ($\Delta x = \Delta y = 500$ m): (a) Kirishima, (b) Unzen, (c) Bandai, and (d) Iwate. W values (Equation 7) in individual grids with more than five rays are plotted using the color scale shown at the bottom of each map. The gray triangles in Figure 10a are the locations of Shimoe-dake (Sm) and Ohachi (Oh) and that in Figure 10b is the location of Fugen-dake, where the 1991 Unzen eruptions occurred.

shallow depths in the eastern and western flanks, respectively, which may correspond to the respective areas of positive and negative residuals (Figure 11d).

These comparisons consistently indicate that areas of positive and negative envelope-width residuals correspond to low- and high-velocity anomalies except for one area near shot location S3 at Kirishima. These correlations suggest that areas of positive residuals correspond to heterogeneous rocks comprising unconsolidated materials and/or fractures, whereas areas of negative residuals correspond to less heterogenous volcanic or basement rocks. To quantify l_0 and Q_i values in these anomalies, a tomographic approach based on inversion of Δp_i^k may prove useful. However, one of the difficulties in performing such an inversion is to construct the data kernel, in which the envelope widths for perturbations of l_0 and Q_i in individual anomalies must be calculated for all combinations of source-station pairs using the Monte Carlo

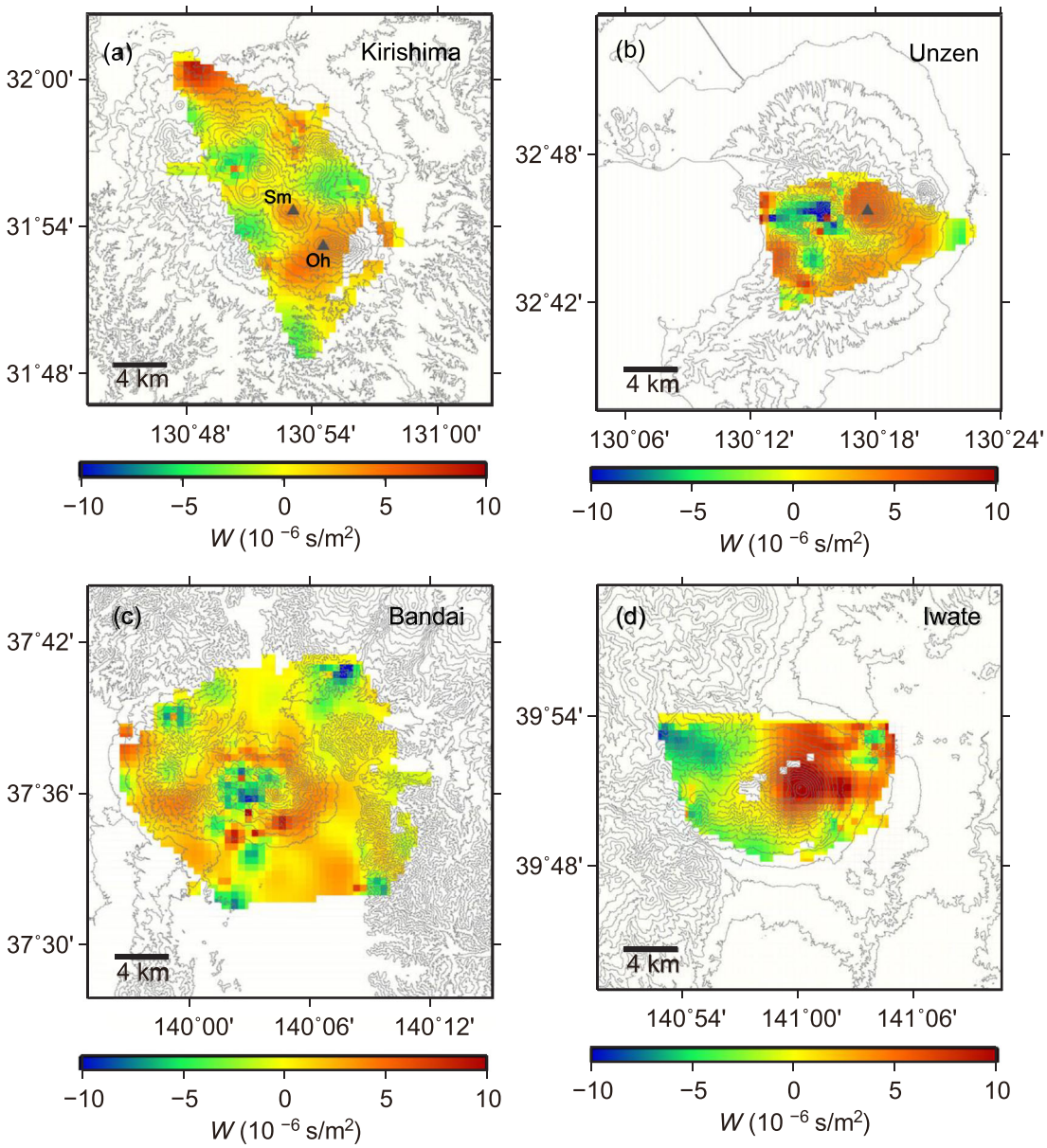

Figure 11. Envelope-width residual maps based on the tomography approach using Equations 7 and 10 ($\Delta x = \Delta y = 500$ m): (a) Kirishima, (b) Unzen, (c) Bandai, and (d) Iwate. Symbols as in Figure 10.

method, which is computationally expensive. Takeuchi (2016) developed an efficient method for calculating envelope seismograms and their partial derivatives with the Monte Carlo method, which was applied to estimate 3D scattering and attenuation structures in the lithosphere in southwest Japan (Ogiso, 2019). However, this method uses the Born approximation assuming single scattering; therefore, it is not applicable to the simulation of seismograms at volcanoes, where multiple scattering dominates at shallow depths. Akande et al. (2019) used 3D sensitivity kernels based on the analytical equation of Paasschens (1997) for attenuation imaging at Campi Flegrei caldera (Italy). This approach was also used by Shito et al. (2020) to estimate scattering and attenuation structures beneath Kyushu, Japan. The 3D kernels, however, are based on uniform l_0 and Q_i distributions, but the assumption of uniform l_0 and Q_i is not appropriate at volcanoes. Future studies should therefore develop a tomographic method with efficient

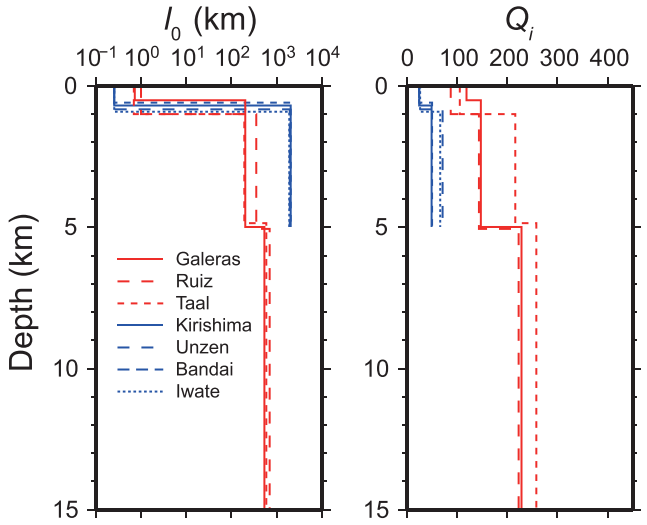

Figure 12. Comparison of estimated 1D models at various volcanoes. Red and blue lines indicate models based on VT earthquakes and active sources, respectively. Models at Nevado del Ruiz (Ruiz) and Taal are from Kumagai et al. (2018).

calculations of partial derivatives of Δp_l^k to estimate 3D l_0 and Q_i distributions beneath volcanoes, which would contribute to our better understanding of magmatic and hydrothermal systems.

5. Conclusions

The envelope widths of VT earthquakes at Galeras and active sources produced by dynamite blasts at Kirishima, Unzen, Bandai, and Iwate were estimated by using high-frequency (5–10 Hz) seismograms. We compared the observed envelope widths with those simulated by the Monte Carlo method and estimated the 1D l_0 and Q_i models at each volcano using the grid-search approach of Kumagai et al. (2018). Our models indicated the existence of a heterogeneous (l_0 = 250–710 m) and attenuative (Q_i = 25–120) surface layer with a thickness of 500–900 m, which is underlain by less heterogeneous layers ($l_0 = 10^2$–10^3 km and Q_i = 50–200). This feature is similar to those found at Vesuvius (Wegler, 2004), Taal, and Nevado del Ruiz (Kumagai et al., 2018), indicating that such strong structural heterogeneities at volcanoes are surface characteristics. These surface layers correspond to low-velocity and low-resistive surface layers that may consist of unconsolidated and/or highly fractured materials, hydrothermal fluids, and altered clay minerals.

Using the 2D SWF of Del Pezzo et al. (2006), we mapped the residuals between the observed envelope widths and those calculated with the best fit layered models at Kirishima, Unzen, Bandai, and Iwate. These maps show areas of negative and positive residuals distributed beneath the volcano flanks at Kirishima, an area of strong negative residuals at Unzen, distinct areas of negative and positive residuals at Bandai, and broad areas of positive and negative residuals in the eastern and western flanks of Iwate, respectively. The spatial distributions of these residuals correlate with *P* wave velocity tomographic images at each volcano: Areas of positive residuals correspond to low-velocity anomalies and thus heterogeneous, strongly scattering rocks, whereas areas of negative residuals correspond to high-velocity anomalies and thus less heterogeneous volcanic or basement rocks. To quantify l_0 and Q_i values in these anomalies, a tomographic approach based on inversion of the envelope-width residuals may prove useful, but it would require an efficient method to calculate envelope seismograms and their partial derivatives with respect to l_0 and Q_i perturbations. Our study demonstrates that the envelope width is useful for improving the characterization of scattering and attenuation structures beneath volcanoes.

Data Availability Statement

Observed and simulated envelope widths and source and station information for our studied volcanoes are found online (http://www.eps.nagoya-u.ac.jp/~kumagai/2020JB020249.zip). Waveform data at Galeras and those at Kirishima, Unzen, Bandai, and Iwate are available upon request from the Colombian Geological Survey (https://www2.sgc.gov.co/Paginas/servicio-geologico-colombiano.aspx) and the Earthquake Research Institute, The University of Tokyo (http://www.eri.u-tokyo.ac.jp/kyodoriyou/facilities/), respectively.

Acknowledgments

We thank Jun Oikawa, Tomoki Tsutsui, Takeshi Matsushima, and Satoshi Tanaka for sharing digital data of seismograms, station locations, source information, and velocity models used in our analysis of active sources. We are grateful to Edoardo Del Pezzo for his advice and information about the space-weighting function. Comments from Luca De Siena and Janire Prudencio were very useful in improving the manuscript. This work was financially supported by JSPS KAKENHI grant 19KK0084 and JST/JICA SATREPS.

References

Aizawa, K., Ogawa, Y., Hashimoto, T., Koyama, T., Kanda, W., Yamaya, Y., et al. (2008). Shallow resistivity structure of Asama Volcano and its implications for magma ascent process in the 2004 eruption. *Journal of Volcanology and Geothermal Research*, *173*, 165–177. https://doi.org/10.1016/j.jvolgeores.2008.01.016

Akande, W. G., De Siena, L., & Gana, Q. (2019). Three-dimensional kernel-based coda attenuation imaging of caldera structures controlling the 1982–84 Campi Flegrei unrest. *Journal of Volcanology and Geothermal Research*, *381*, 273–283. https://doi.org/10.1016/j.jvolgeores.2019.06.007

Alanis, P. K. B., Yamaya, Y., Takeuchi, A., Sasai, Y., Okada, U., & Nagao, T. (2013). A large hydrothermal reservoir beneath Taal Volcano (Philippines) revealed by magnetotelluric observations and its implications to the volcanic activity. *Proceedings of the Japan Academy, Series B*, *89*, 383–389. https://doi.org/10.2183/pjab.89.383

Aoki, Y., Takeo, M., Aoyama, H., Fujimatsu, J., Matsumoto, S., Miyamachi, H., et al. (2009). P-wave velocity structure beneath Asama Volcano, Japan, inferred from active source seismic experiment. *Journal of Volcanology and Geothermal Research*, *187*, 272–277. https://doi.org/10.1016/j.jvolgeores.2009.09.004

Bain, A. A., Calder, E. S., Cortés, J. A., Cortés, G. P., & Loughlin, S. C. (2019). Textural and geochemical constraints on andesitic plug emplacement prior to the 2004-2010 vulcanian explosions at Galeras volcano, Colombia. *Bulletin of Volcanology*, *81*, 1. https://doi.org/10.1007/s00445-018-1260-y

Battaglia, J., & Aki, K. (2003). Location of seismic events and eruptive fissures on the Piton de la Fournaise volcano using seismic amplitudes. *Journal of Geophysical Research*, *108*(B10), 2364. https://doi.org/10.1029/2002JB002193

Benz, H., Chouet, B., Dawson, P. B., Lahr, J. C., Page, R. A., & Hole, J. A. (1996). Three-dimensional P and S wave velocity structure of Redoubt Volcano, Alaska. *Journal of Geophysical Research*, *101*(B4), 8111–8128. https://doi.org/10.1029/95JB03046

Calvache, M. L., & Williams, S. N. (1997). Emplacement and petrological evolution of the andesitic dome of Galeras volcano, 1990–1992. *Journal of Volcanology and Geothermal Research*, *77*, 57–69. https://doi.org/10.1016/S0377-0273(96)00086-8

Carcolé, E., Ugalde, A., & Vargas, C. A. (2006). Three-dimensional spatial distribution of scatterers in Galeras volcano, Colombia. *Geophysical Research Letters*, *33*, L08307. https://doi.org/10.1029/2006GL025751

Caudron, C., White, R. S., Green, R. G., Woods, J., Ágústsdóttir, T., Donaldson, C., et al. (2018). Seismic amplitude ratio analysis of the 2014–2015 Bárðarbunga-Holuhraun dike propagation and eruption. *Journal of Geophysical Research: Solid Earth*, *123*, 264–276. https://doi.org/10.1002/2017JB014660

Chouet, B. A., & Matoza, R. S. (2013). A multi-decadal view of seismic methods for detecting precursors of magma movement and eruption. *Journal of Volcanology and Geothermal Research*, *252*, 108–175. https://doi.org/10.1016/j.jvolgeores.2012.11.013

De Siena, L., Amoruso, A., Del Pezzo, E., Wakeford, Z., Castellano, M., & Crescentini, L. (2017). Space-weighted seismic attenuation mapping of the aseismic source of Campi Flegrei 1983–1984 unrest. *Geophysical Research Letters*, *44*, 1740–1748. https://doi.org/10.1002/2017GL072507

De Siena, L., Calvet, M., Watson, K. J., Jonkers, A. R. T., & Thomas, C. (2016). Seismic scattering and absorption mapping of debris flows, feeding paths, and tectonic units at Mount St. Helens volcano. *Earth and Planetary Science Letters*, *442*, 21–31. https://doi.org/10.1016/j.epsl.2016.02.026

Del Pezzo, E., Bianco, F., & Zaccarelli, L. (2006). Separation of Q_i and Q_s from passive data at Mt. Vesuvius: A reappraisal of the seismic attenuation estimates. *Physics of the Earth and Planetary Interiors*, *159*, 202–212. https://doi.org/10.1016/j.pepi.2006.07.005

Del Pezzo, E., De La Torre, A., Bianco, F., Ibanez, J., Gabrielli, S., & De Siena, L. (2018). Numerically calculated 3D space-weighting functions to image crustal volcanic structures using diffuse coda waves. *Geosciences*, *8*, 175. https://doi.org/10.3390/geosciences8050175

Del Pezzo, E., Ibañez, J., Prudencio, J., Bianco, F., & De Siena, L. (2016). Absorption and scattering 2-D volcano images from numerically calculated space-weighting functions. *Geophysical Journal International*, *206*, 742–756. https://doi.org/10.1093/gji/ggw171

Friedrich, C., & Wegler, U. (2005). Localization of seismic coda at Merapi volcano (Indonesia). *Geophysical Research Letters*, *32*, L14312. https://doi.org/10.1029/2005GL023111

Gabrielli, S., De Siena, L., Napolitano, F., & Del Pezzo, E. (2020). Understanding seismic path biases and magmatic activity at Mount St Helens volcano before its 2004 eruption. *Geophysical Journal International*, *222*, 169–188. https://doi.org/10.1093/gji/ggaa154

Gil Cruz, F., & Chouet, B. A. (1997). Long-period events, the most characteristic seismicity accompanying the emplacement and extrusion of a lava dome in Galeras Volcano, Colombia, in 1991. *Journal of Volcanology and Geothermal Research*, *77*(1–4), 121–158. https://doi.org/10.1016/S0377-0273(96)00091-1

Hoshizumi, H., Uto, K., & Watanabe, K. (1999). Geology and eruptive history of Unzen volcano, Shimabara Peninsula, Kyushu, SW Japan. *Journal of Volcanology and Geothermal Research*, *89*, 81–94. https://doi.org/10.1016/S0377-0273(98)00125-5

Ichihara, M. (2016). Seismic and infrasonic eruption tremors and their relation to magma discharge rate: A case study for sub-Plinian events in the 2011 eruption of Shinmoe-dake, Japan. *Journal of Geophysical Research: Solid Earth*, *121*, 7101–7118. https://doi.org/10.1002/2016JB013246

Ichihara, M., & Matsumoto, S. (2017). Relative source locations of continuous tremor before and after the Subplinian events at Shinmoe-dake, in 2011. *Geophysical Research Letters*, *44*, 10,871–10,877. https://doi.org/10.1002/2017GL075293

Ichimura, M., Yokoo, A., Kagiyama, T., Yoshikawa, S., & Inoue, H. (2018). Temporal variation in source location of continuous tremors before ash–gas emissions in January 2014 at Aso volcano, Japan. *Earth, Planets and Space*, *70*, 125. https://doi.org/10.1186/s40623-018-0895-4

Kagiyama, T., Tsutsui, T., Mikada, H., Morita, Y., Matsushima, T., & Iguchi, M. (1995). 1994 explosion experiment in Kirishima volcanoes. *Bulletin of the Earthquake Research Institute*, *70*, 33–60.

Kanda, W., Tanaka, Y., Utsugi, M., Takakura, S., Hashimoto, T., & Inoue, H. (2008). A preparation zone for volcanic explosions beneath Naka-dake crater, Aso volcano, as inferred from magnetotelluric surveys. *Journal of Volcanology and Geothermal Research*, *178*, 32–45. https://doi.org/10.1016/j.jvolgeores.2008.01.022

Koulakov, I., Gordeev, E. I., Dobretsov, N. L., Vernikovsky, V. A., Senyukov, S., Jakovlev, A., & Jaxybulatov, K. (2013). Rapid changes in magma storage beneath the Klyuchevskoy group of volcanoes inferred from time-dependent seismic tomography. *Journal of Volcanology and Geothermal Research*, *263*, 75–91. https://doi.org/10.1016/j.jvolgeores.2012.10.014

Koulakov, I., & Shapiro, N. (2015). Seismic tomography of volcanoes. In *Encyclopedia of Earthquake Engineering*. Heidelberg: Springer-Verlag Berlin. https://doi.org/10.1007/978-3-642-36197-5_51-1

Kozono, T., Ueda, H., Shimbori, T., & Fukui, K. (2014). Correlation between magma chamber deflation and eruption cloud height during the 2011 Shinmoe-dake eruptions. *Earth, Planets and Space*, *66*, 1–8. https://doi.org/10.1186/s40623-014-0139-1

Kumagai, H., Lacson, R. Jr., Maeda, Y., Figueroa, M. S. II, Yamashina, T., Ruiz, M., et al. (2013). Source amplitudes of volcano-seismic signals determined by the amplitude source location method as a quantitative measure of event size. *Journal of Volcanology and Geothermal Research*, *257*, 57–71. https://doi.org/10.1016/j.jvolgeores.2013.03.002

Kumagai, H., Londoño, J. M., Maeda, Y., & Acevedo Rivas, A. E. (2019). Amplitude source location method with depth-dependent scattering and attenuation structures: Application at Nevado del Ruiz volcano, Colombia. *Journal of Geophysical Research: Solid Earth*, *124*, 422. https://doi.org/10.1029/2019JB018156

Kumagai, H., Londoño, J. M., Maeda, Y., López Velez, C. M., & Lacson, R. Jr. (2018). Envelope widths of volcano-seismic events and seismic scattering characteristics beneath volcanoes. *Journal of Geophysical Research: Solid Earth*, *123*, 9764–9777. https://doi.org/10.1029/2018JB015557

Kumagai, H., Nakano, M., Maeda, T., Yepes, H., Palacios, P., Ruiz, M., et al. (2010). Broadband seismic monitoring of active volcanoes using deterministic and stochastic approaches. *Journal of Geophysical Research*, *115*, B08303. https://doi.org/10.1029/2009JB006889

Kurokawa, A., Takeo, M., & Kurita, K. (2016). Two types of volcanic tremor changed with eruption style during 1986 Izu-Oshima eruption. *Journal of Geophysical Research: Solid Earth*, *121*, 2727–2736. https://doi.org/10.1002/2015JB012500

Lees, J. M. (2007). Seismic tomography of magmatic systems. *Journal of Volcanology and Geothermal Research*, *167*, 37–56. https://doi.org/10.1016/j.jvolgeores.2007.06.008

Londoño, J. M., & Kumagai, H. (2018). 4D seismic tomography of Nevado del Ruiz volcano, Colombia, 2000–2016. *Journal of Volcanology and Geothermal Research*, *358*, 105–123. https://doi.org/10.1016/j.jvolgeores.2018.02.015

Maeda, Y., Takeo, M., & Kazahaya, R. (2019). Comparison of high- and low-frequency signal sources for very-long-period seismic events at Asama volcano, Japan. *Geophysical Journal International*, *217*, 389–404. https://doi.org/10.1093/gji/ggz021

Matsushima, T., Iguchi, M., Nishimura, Y., Kagiyama, T., Watanabe, H., & Mikada, H. (1995). GPS survey of shot and observation points in the explosion experiment of Kirishima-1994. *Bulletin of the Earthquake Research Institute*, *70*, 61–68.

Matsushima, T., Shimizu, H., Nishimura, Y., Ueki, S., Nishimura, T., & Aoki, S. (1997). 1995 Explosion experiment in Unzen Volcano. *Bulletin of the Earthquake Research Institute*, *72*, 167–183.

Menke, H. (1989). *Geophysical data analysis: Discrete inverse theory* (). San Diego, CA: Academic Press.

Miura, S., Ueki, S., Sato, T., Tachibana, K., & Hamaguchi, H. (2000). Crustal deformation associated with the 1998 seismo-volcanic crisis of Iwate volcano, northeastern Japan, as observed by a dense GPS network. *Earth, Planets and Space*, *52*, 1003–1008. https://doi.org/10.1186/BF03352321

Molina, I., Kumagai, H., Le Penneca, J. -L., & Hall, M. (2005). Three-dimensional P-wave velocity structure of Tungurahua Volcano, Ecuador. *Journal of Volcanology and Geothermal Research*, *147*, 144–156. https://doi.org/10.1016/j.jvolgeores.2005.03.011

Mori, A., & Kumagai, H. (2019). Estimating plume heights of explosive eruptions using high-frequency seismic amplitudes. *Geophysical Journal International*, *219*, 1365–1376. https://doi.org/10.1093/gji/ggz374

Morioka, H., Kumagai, H., & Maeda, T. (2017). Theoretical basis of the amplitude source location method for volcano-seismic signals. *Journal of Geophysical Research: Solid Earth*, *122*, 6538–6551. https://doi.org/10.1002/2017JB013997

Nakada, S., Nagai, M., Kaneko, T., Suzuki, Y., & Maeno, F. (2013). The outline of the 2011 eruption at Shinmoe-dake (Kirishima), Japan. *Earth, Planets and Space*, *65*, 475–488. https://doi.org/10.5047/eps.2013.03.016

Nakada, S., Shimizu, H., & Ohta, K. (1999). Overview of the 1990–1995 eruption at Unzen Volcano. *Journal of Volcanology and Geothermal Research*, *89*, 1–22. https://doi.org/10.1016/S0377-0273(98)00118-8

Nakamura, Y. (1978). Geology and petrology of Bandai and Nekoma Volcanoes. *Science Reports of the Tohoku University 3rd Ser.*, *3*(14), 67–119.

Nishi, K. (2002). Three-dimensional seismic velocity structure beneath Unzen volcano, Kyushu, Japan inferred by tomography from experimental explosion data. *Bulletin of the Volcanological Society of Japan*, *47*, 227–241. https://doi.org/10.18940/kazan.47.4_227

Nishigami, K. (1991). A new inversion method of coda waveforms to determine spatial distribution of coda scatterers in the curst and upper most mantle. *Geophysical Research Letters*, *18*, 2225–2228. https://doi.org/10.1029/91GL02823

Nishimura, T., Nakamichi, H., Tanaka, S., Sato, M., Kobayashi, T., Ueki, S., et al. (2000). Source process of very long period seismic events associated with the 1998 activity of Iwate volcano, northeastern Japan. *Journal of Geophysical Research*, *105*(B8), 19,135–19,147. https://doi.org/10.1029/2000JB900155

Nurhasan, Y. O., Ujihara, N., Bulent Tank, S., Honkura, Y., Onizawa, S., et al. (2006). Two electrical conductors beneath Kusatsu-Shirane volcano, Japan, imaged by audiomagnetotellurics, and their implications for the hydrothermal system. *Earth, Planets and Space*, *58*, 1053–1059. https://doi.org/10.1186/BF03352610

Obara, K., & Sato, H. (1995). Regional differences of random inhomogeneities around the volcanic front in the Kanto-Tokai area, Japan, revealed from the broadening of *S* wave seismogram envelopes. *Journal of Geophysical Research*, *100*(B2), 2103–2121. https://doi.org/10.1029/94JB02644

Ogiso, M. (2019). A method for mapping intrinsic attenuation factors and scattering coefficients of S waves in 3-D space and its application in southwestern Japan. *Geophysical Journal International*, *216*, 948–957. https://doi.org/10.1093/gji/ggy468

Ogiso, M., & Yomogida, K. (2015). Estimation of locations and migration of debris flows on Izu-Oshima Island, Japan. *Journal of Volcanology and Geothermal Research*, *298*, 15–26. https://doi.org/10.1016/j.jvolgeores.2015.03.015

Paasschens, J. C. J. (1997). Solution of the time-dependent Boltzmann equation. *Physical Review E*, *56*, 1135–1141. https://doi.org/10.1103/PhysRevE.56.1135

Parsiegla, N., & Wegler, U. (2008). Modelling of seismic energy transport at volcanoes with real topography and complex propagation medium. *Journal of Volcanology and Geothermal Research*, *171*, 229–236. https://doi.org/10.1016/j.jvolgeores.2007.12.001

Patanè, D., Barberi, G., Cocina, O., De Gori, P., & Chiarabba, C. (2006). Time-resolved seismic tomography detects magma intrusions at Mount Etna. *Science*, *303*, 313–321. https://doi.org/10.1126/science.1127724

Pérez-Guillén, C., Tsunematsu, K., Nishimura, K., & Issler, D. (2019). Seismic location and tracking of snow avalanches and slush flows on Mt. Fuji, Japan. *Earth Surface Dynamics*, *7*, 989–1007. https://doi.org/10.5194/esurf-7-989-2019

Podvin, P., & Lecomte, I. (1991). Finite difference computation of travel-times in very contrasted velocity models: A massively parallel approach and its associated tools. *Geophysical Journal International*, *105*, 271–284. https://doi.org/10.1111/j.1365-246X.1991.tb03461.x

Prudencio, J., Aoki, Y., Takeo, M., Ibáñez, J. M., Del Pezzo, E., & Song, W. (2017). Separation of scattering and intrinsic attenuation at Asama volcano (Japan): Evidence of high volcanic structural contrasts. *Journal of Volcanology and Geothermal Research*, *333-334*, 96–103. https://doi.org/10.1016/j.jvolgeores.2017.01.014

Prudencio, J., Del Pezzo, E., García-Yeguas, A., & Ibáñez, J. M. (2013). Spatial distribution of intrinsic and scattering seismic attenuation in active volcanic islands—I: Model and the case of Tenerife Island. *Geophysical Journal International*, *195*, 1942–1956. https://doi.org/10.1093/gji/ggt361

Prudencio, J., Del Pezzo, E., Ibáñez, J. M., Giampiccolo, E., & Patanè, D. (2015). Two-dimensional seismic attenuation images of Stromboli Island using active data. *Geophysical Research Letters*, *42*, 1717–1724. https://doi.org/10.1002/2015GL063293

Prudencio, J., Ibáñez, J. M., García-Yeguas, A., Del Pezzo, E., & Posadas, A. M. (2013). Spatial distribution of intrinsic and scattering seismic attenuation in active volcanic islands—II: Deception Island images. *Geophysical Journal International*, *195*, 1957–1969. https://doi.org/10.1093/gji/ggt360

Prudencio, J., Taira, T., Aoki, Y., Aoyama, H., & Onizawa, S. (2017). Intrinsic and scattering attenuation images of Usu volcano, Japan. *Bulletin of Volcanology*, *79*, 29. https://doi.org/10.1007/s00445-017-1117-9

Saito, T., Sato, H., & Ohtake, M. (2005). Unified explanation of envelope broadening and maximum amplitude decay of high-frequency seismograms based on the envelope simulation using the Markov approximation: Forearc side of the volcanic front in northeastern Honshu, Japan. *Journal of Geophysical Research*, *110*, B01304. https://doi.org/10.1029/2004JB003225

Sato, H., Fehler, M. C., & Maeda, T. (2012). *Seismic wave propagation and scattering in the heterogeneous Earth*. New York, NY: Springer.
Sato, H., Fujii, T., & Nakada, S. (1992). Crumbling of dacite dome lava and generation of pyroclastic flows at Unzen volcano. *Nature*, *360*, 664–666. https://doi.org/10.1038/360664a0
Sekiya, S., & Kikuchi, Y. (1889). The eruption of Bandai-san. *Journal of the College of Science, Imperial University of Tokyo*, *3*, 91–172.
Shimbori, T., Sakurai, T., Tahara, M., & Fukui, K. (2013). Observation of eruption clouds with weather radars and meteorological satellites: A case study of the eruptions at Shinmoedake volcano in 2011. *Quarterly Journal of Seismology*, *77*, 139–214.
Shito, A., Matsumoto, S., Ohkura, T., Shimizu, H., Sakai, S., Iio, Y., et al. (2020). 3-D intrinsic and scattering seismic attenuation structures beneath Kyushu, Japan. *Journal of Geophysical Research: Solid Earth*, *125*, e2019JB018742. https://doi.org/10.1029/2019JB018742
Sketsiou, P., Napolitano, F., Zenonos, A., & De Siena, L. (2020). New insights into seismic absorption imaging. *Physics of the Earth and Planetary Interiors*, *298*, 106337. https://doi.org/10.1016/j.pepi.2019.106337
Stix, J., Torres, C. R., Narvaez, M. L., Cortes, J. G. P., Raigosa, J. A., Gomez, M. D., & Castonguay, R. (1997). A model of vulcanian eruptions at Galeras volcano, Colombia. *Journal of Volcanology and Geothermal Research*, *77*(1–4), 285–303. https://doi.org/10.1016/S0377-0273(96)00100-X
Taisne, B., Brenguier, F., Shapiro, N. M., & Ferrazzini, V. (2011). Imaging the dynamics of magma propagation using radiated seismic intensity. *Geophysical Research Letters*, *38*, L04304. https://doi.org/10.1029/2010GL046068
Takahashi, T., Sato, H., Nishimura, T., & Obara, K. (2007). Strong inhomogeneity beneath Quaternary volcanoes revealed from the peak delay analysis of *S*-wave seismograms of microearthquakes in northeastern Japan. *Geophysical Journal International*, *168*, 90–99. https://doi.org/10.1111/j.1365-246X.2006.03197.x
Takeuchi, N. (2016). Differential Monte Carlo method for computing seismogram envelopes and their partial derivatives. *Journal of Geophysical Research: Solid Earth*, *121*, 3428–3444. https://doi.org/10.1002/2015JB012661
Tan, C. T., Taisne, B., Neuberg, J., & Basuki, A. (2019). Real-time assessment of potential seismic migration within a monitoring network using Red-flag SARA. *Journal of Volcanology and Geothermal Research*, *384*, 31–47. https://doi.org/10.1016/0377-0273(90)90027-D
Tanaka, S., Hamaguchi, H., Nishimura, T., Yamawaki, T., Ueki, S., Nakamichi, H., et al. (2002). Three-dimensional P-wave velocity structure of Iwate volcano, Japan from active seismic survey. *Geophysical Research Letters*, *29*(10), 1420. https://doi.org/10.1029/2002GL014983
Tanaka, S., Hamaguchi, H., Yamawaki, T., Nishimura, T., Ueki, S., Nakamichi, H., et al. (2002). Seismic exploration at Iwate volcano with active sources—The outline of the experiment and the first arrival data. *Bulletin of the Earthquake Research Institute*, *77*(1).
Tomatsu, T., Kumagai, H., & Dawson, P. B. (2001). Tomographic inversion of *P*-wave velocity and *Q* structures beneath the Kirishima volcanic complex, southern Japan, based on finite-difference calculations of complex traveltimes. *Geophysical Journal International*, *146*, 781–794. https://doi.org/10.1016/j.jvolgeores.2019.07.004
Tomatsu, T., Kumagai, H., Kunitomo, T., Yamaoka, K., & Watanabe, T. (1997). Subsurface velocity structure under the Kirishima Volcanoes inferred from explosion seismic observations. *Bulletin of the Volcanological Society of Japan*, *42*, 159–163. https://doi.org/10.18940/kazan.42.2_159
Torres, R. A., Gómez, D. M., & Narváez, L. (1996). Unusual seismic signals associated with the activity at Galeras volcano, Colombia, from July 1992 to September 1994. *Annali di Geofisica*, *39*, 1–12. https://doi.org/10.4401/ag-3975
Tripathi, J. N., Sato, H., & Yamamoto, M. (2010). Envelope broadening characteristics of crustal earthquakes in northeastern Honshu, Japan. *Geophysical Journal International*, *182*, 988–1000. https://doi.org/10.1111/j.1365-246X.2010.04657.x
Tsutsui, T., Kagiyama, T., Morita, Y., Matsushima, T., Iguchi, M., Yamaoka, K., et al. (1996). Seismic velocity structure beneath Kirishima Volcanoes with differential analysis of explosion experiment. *Bulletin of the Volcanological Society of Japan*, *41*, 227–241. https://doi.org/10.18940/kazan.41.5_227
Walter, F., Burtin, A., McArdell, B. W., Hovius, N., Weder, B., & Turowski, J. M. (2017). Testing seismic amplitude source location for fast debris-flow detection at Illgraben, Switzerland. *Natural Hazards and Earth System Sciences*, *17*, 939–955. https://doi.org/10.5194/nhess-17-939-2017
Wegler, U. (2003). Analysis of multiple scattering at Vesuvius volcano, Italy, using data of the TomoVes active seismic experiment. *Journal of Volcanology and Geothermal Research*, *128*, 45–63. https://doi.org/10.1016/S0377-0273(03)00246-4
Wegler, U. (2004). Diffusion of seismic waves in a thick layer: Theory and application to Vesuvius volcano. *Journal of Geophysical Research*, *109*, B07303. https://doi.org/10.1029/2004JB003048
Wegler, U., & Lühr, B.-G. (2001). Scattering behaviour at Merapi volcano (Java) revealed from an active seismic experiment. *Geophysical Journal International*, *145*, 579–592. https://doi.org/10.1046/j.1365-246x.2001.01390.x
Yamamoto, M., & Sato, H. (2010). Multiple scattering and mode conversion revealed by an active seismic experiment at Asama volcano, Japan. *Journal of Geophysical Research*, *115*, B07304. https://doi.org/10.1029/2009JB007109
Yamasato, H. (1997). Quantitative analysis of pyroclastic flows using infrasonic and seismic data at Unzen Volcano, Japan. *Journal of Physics of the Earth*, *45*, 397–416. https://doi.org/10.4294/jpe1952.45.397
Yamasato, T., Takarada, S., & Suto, S. (1993). Pyroclastic flows from the 1991 eruption of Unzen volcano, Japan. *Bulletin of Volcanology*, *55*, 166–175. https://doi.org/10.1007/BF00301514
Yamawaki, T., Tanaka, S., Ueki, S., Hamaguchi, H., Nakamichi, H., Nishimura, T., et al. (2004). Three-dimensional *P*-wave velocity structure of Bandai volcano in northeastern Japan inferred from active seismic survey. *Journal of Volcanology and Geothermal Research*, *138*, 267–282. https://doi.org/10.1016/j.jvolgeores.2004.07.010
Yamaya, Y., Alanis, P. K. B., Takeuchi, A., Cordon, J. M. Jr., Mogi, T., Hashimoto, T., et al. (2013). A large hydrothermal reservoir beneath Taal Volcano (Philippines) revealed by magnetotelluric resistivity survey: 2D resistivity modeling. *Bulletin of Volcanology*, *75*, 7–13. https://doi.org/10.1007/s00445-013-0729-y
Yoshimoto, K. (2000). Monte Carlo simulation of seismogram envelopes in scattering media. *Journal of Geophysical Research*, *105*(B3), 6153–6161. https://doi.org/10.1029/1999JB900437
Zollo, A., Judenherc, S., Auger, E., D'Auria, L., Virieux, J., & Capuano, P. (2003). Evidence for the buried rim of Campi Flegrei caldera from 3-d active seismic imaging. *Geophysical Research Letters*, *30*(19), 2002. https://doi.org/10.1029/2003GL018173